Main Manuscript for

Synchronicity transitions determine coupling fluctuations in a model of coupled oscillators with plasticity

Satoshi Kuroki [a*] and Kenji Mizuseki [a]

[a] Department of Physiology, Osaka Metropolitan University Graduate School of Medicine, Asahimachi 1-4-3, Abeno-ku, Osaka, 545-8585, Japan, +81-6-6645-3717

* Satoshi Kuroki, Department of Physiology, Osaka Metropolitan University Graduate School of Medicine, Asahimachi 1-4-3, Abeno-ku, Osaka, 545-8585, Japan, +81-6-6645-3717, skuroki@omu.ac.jp

Email: skuroki@omu.ac.jp

Author Contributions: S.K.: Conceptualization, Investigation, Visualization, Writing - original draft, Writing – review and editing, Funding acquisition; K.M.: Supervision, Writing – review and editing, Funding acquisition

Competing Interest Statement: The authors declare that they have no known competing financial interests or personal relationships that could have appeared to influence the work reported in this paper.

Classification: Systems Neuroscience

Keywords: Network reorganization, Plasticity, EI balance, Synchronization

This PDF file includes:

Main Text
Figures 1 to 5

Abstract

Sleep and rest are crucial to knowledge abstraction and creativity. During these periods, synapses undergo plastic modification, while neuronal activities are collectively synchronized, accompanied by large shifts in the excitation-inhibition (EI) balance. These phenomena differ from the learning processes that occur during task engagement. However, the detailed mechanism by which synchronized neuronal activity reshapes neural circuits through plasticity is not yet fully understood. The Kuramoto model is used to study the collective synchronization of oscillators, including neurons. We previously proposed the EI-Kuramoto model, in which an EI balance was implemented in the Kuramoto model. The model alters its synchronicity based on the EI balance of the interaction strength. In this study, we further developed the EI-Kuramoto model by implementing Hebbian and homeostatic plasticity, leading to a plastic EI-Kuramoto (pEI-Kuramoto) model. Models with robust inhibition consistently showed desynchronization and stable coupling. Contrastingly, weaker inhibition produced bistable synchronization, in which couplings with intermediate strengths fluctuated, whereas the strongest couplings remained stable. Our findings suggest that the dynamic interplay between network activity and plasticity explains why stronger synapses in the brain exhibit greater stability than their weaker counterparts. Moreover, this mechanism facilitated network reorganization during sleep and rest.

Significance Statement

The reorganization of neuronal circuits during sleep and rest is essential for knowledge abstraction and creativity. These states involve synaptic plasticity and collective neuronal synchronization, accompanied by significant shifts in the excitation-inhibition (EI) balance. However, the precise mechanism through which synchronized activity reshapes neural circuits via plasticity remains unclear. We developed a novel computational model, the pEI-Kuramoto model, which incorporates both coupling plasticity and EI balance. Our model demonstrates that robust inhibition leads to desynchronization and stable coupling. In contrast, weaker inhibition induces bistable synchronization, in which the intermediate-strength couplings fluctuate, whereas the strongest couplings remain stable. These findings provide a fundamental mechanism for network reorganization during sleep and at rest.

Main Text

Introduction

Empirical evidence suggests that brain activity during sleep and rest promotes memory consolidation, abstraction of knowledge, and the creation of new ideas (1, 2) through the reorganization of neural circuits (3, 4). This reorganization should differ from learning while performing a task. Indeed, synaptic plasticity during sleep and rest improves task performance (5, 6).

Neuronal synchronization occurs in two distinct states. Collective neuronal firing is desynchronized during active wakefulness, including task engagement, movement, and attentional states, as well as during rapid eye movement (REM) sleep, which are referred to as brain-activated states. Contrastingly, neuronal firing synchronizes during non-REM sleep and quiet wakefulness, which are referred to as brain-deactivated states (7, 8). The transition between these states is associated with shifts in the excitation-inhibition (EI) balance. Firing rates of inhibitory neurons and synaptic conductance of inhibitory synapses are significantly elevated during brain-activated states, while those of excitatory synapses show comparatively smaller changes (9–12). These observations suggest that the extent to which collective neuronal synchronization is accompanied by EI balance and synaptic plasticity during brain-deactivated states can influence network reorganization. However, the detailed mechanisms by which

neuronal synchronization in the brain-deactivated state reshapes the neural network structure remain unclear.

The collective synchronization of oscillators, including neurons, has been studied using a model of coupled oscillators. Among these, the Kuramoto model is considered to be the simplest framework (13, 14), and numerous variants have been proposed. One variant, the EI-Kuramoto model, captures the EI balance by dividing oscillators into excitatory and inhibitory groups and assigning four interaction types between them (15, 16). We have previously shown that tuning these four strengths toggles the network between synchronized, desynchronized, and bistable states, potentially reflecting a neuronal synchronization mechanism (16). That study, however, kept all coupling weight—which represent pair-specific interaction strengths—fixed and identical, and therefore did not address how the EI balance and its associated dynamical states influence plastic changes in the coupling weights.

In this study, we focused on Hebbian and homeostatic plasticities. Hebbian plasticity, based on the principle “fire together, wire together,” strengthens synapses between neurons that fire in close temporal proximity (17). However, homeostatic plasticity regulates neuronal excitability and synaptic strength to maintain network stability, thereby preventing excessive excitation or quiescence (18). The interplay between these plasticity mechanisms enables the emergence of diverse neuronal functions and firing patterns (19–22). Several Kuramoto model studies have implemented plasticity, enabling coupling weights to adapt based on the oscillator activity to examine their impact on system synchronization (23–33).

In this study, we refined the EI-Kuramoto model by integrating Hebbian and homeostatic plasticity into the coupling weights between excitatory oscillator unit pairs (referred to as plastic EI, pEI-Kuramoto model). We observed that the network maintained robustness and minimal fluctuations when inhibition was strong, corresponding to the desynchronized state. Conversely, with weaker inhibition, corresponding to the bistable state, couplings with moderate weights tended to fluctuate, whereas couplings with strong weights remained stable. These findings on the network dynamics of the pEI-Kuramoto model may provide important insights into the mechanisms of neural networks in a brain-deactivated state.

Results

Establishment of the pEI-Kuramoto model The pEI-Kuramoto model comprised two oscillator groups: excitatory units, referred to as excUnits, and inhibitory units, referred to as inhUnits. These specific terms clarified that units represented excitatory and inhibitory factors in this model, not actual neurons or synapses. Four interaction strengths were assigned between the groups, with only excitatory-excitatory couplings J_{ee} being distributed and plastic. The other constant interaction strengths were represented as K_{ei}, K_{ie}, and K_{ii} (Fig 1A; see Materials and Methods). The interactions, which are modeled as zero phase lag sine functions, are purely attractive within excUnits and purely repulsive within inhUnits. Consequently, the terms "excitatory" and "inhibitory" are used synonymously with "attractive" and "repulsive," respectively.

First, we investigated how the distribution of pair-specific excitatory-excitatory coupling weights J_{ee} without plasticity, affected the dynamics of the pEI-Kuramoto model. In our previous study, we showed that the Kuramoto model with EI balance (EI-Kuramoto model) exhibited three distinct dynamic states—synchronized, bistable, and desynchronized—depending on the balance between the constant values of the interaction strengths (16). In this study, J_{ee} followed a Gaussian distribution with a mean of μ_{Jee} and a standard deviation of σ_{Jee}, where σ_{Jee} was set to 0, 1/10, and 1/2 of μ_{Jee} (Fig. 1B). The collective synchronization was quantified using the order parameter R, which represents the magnitude of the average vector between the oscillator units. Regardless of the standard deviation, all systems with a distributed J_{ee} also exhibited synchronized (high R), bistable (alternating high and low R), and desynchronized (low R) dynamics as observed with constant ($\sigma_{Jee} = 0$) values (Fig. 1C).

Next, we incorporated plasticity into J_{ee} by applying Hebbian potentiation and homeostatic regularization plasticity rules (see Materials and Methods). Among the various methods available for implementing Hebbian plasticity in the Kuramoto model, we initially selected the simplest method: the cosine (or sine) function (SI Appendix, Fig. S1A; see Materials and Methods) (23–25,

28, 32, 33). In this process, when a pair of excUnits exhibits closer phases, their J_{ee} coupling weight is potentiated. Simultaneously, the J_{ee} distribution was rescaled to maintain the initial mean and standard deviation, thereby preventing overpotentiation (homeostatic regularization plasticity; see Materials and Methods). The system dynamics were evaluated using the parameter set (μ_{Jee} = 1, σ_{Jee} = 0.1, K_{ei} = 3, K_{ie} = 3, K_{ii} = 3) at which the system exhibited a desynchronized state in the absence of J_{ee} plasticity. Under the cosine rule, unit pairs with smaller phase differences acquire a larger J_{ee} weight. This rule causes the J_{ee} distribution, which was initially Gaussian, to become bimodal (Fig. S1B). Plasticity also influences the distribution of oscillator units, making the distributions of both phase and phase difference become bimodal (SI Appendix, Fig. S1C), consistent with previous studies that incorporated the Hebbian rule into the Kuramoto model (23, 28). This bimodal distribution of the coupling weight deviates from the long-tailed, skewed distributions commonly observed in biological synaptic weights (12, 34, 35).

To address this discrepancy, we introduced an exponential-based Hebbian plasticity rule to adjust the decay rate (Sparseness γ) of the gain for the phase difference (Fig. 1D). We applied this rule to a range of parameter sets and evaluated the resulting J_{ee} distribution using the skewness, kurtosis, and dip values, which quantifies the distribution bimodality (36). Although these distributions initially followed a Gaussian pattern, they transitioned into various bimodal or skewed forms (Fig. 1E and F). We also quantified synchronization of the excUNits using the mean and standard deviation of the order parameter R_{exc} through time, denoted as $E[R_{exc}]_t$ and $S[R_{exc}]_t$, respectively. Plasticity in J_{ee} affects synchronization (Fig. 1G), resulting in uniform, bimodal, or unimodal phase and phase-difference distributions depending on the parameters (Fig. S1C). Moreover, the boundary of the statistical features of the J_{ee} distribution (Fig 1E) appears to coincide with the synchronization boundary (Fig 1G). For further analysis, we chose a parameter set that resulted in a long-tailed skewed J_{ee} distribution (Fig. 1F, top, magenta circle), which more closely reflects the synaptic weight distributions reported in the brain (12, 34, 35).

Coupling fluctuation increases in bistable synchronization state We then investigated how the dynamic state affects coupling weight, focusing on the role of inhibition, which varies significantly across different brain states (9–12), resulting in changes in EI balance (7, 37). To investigate this, we altered the EI balance of the pEI-Kuramoto model by manipulating the interaction strength of the inhUnits. We integrated K_{ie} and K_{ii} into a single parameter, K_i, to simplify the simulation following the approach used in our previous study (16). We then examined how the J_{ee} fluctuations were associated with the K_i values, quantified as the standard deviation of J_{ee} over time ($S[J_{ee}]_t$; see Materials and Methods). By analyzing the time course of R_{exc}, we determined the dynamic state of the system, as previously described (16).

When $K_i < 0.4$, both the average $S[J_{ee}]_t$ across the unit pairs ($E\{S[J_{ee}]_t\}_n$) and the standard deviation of $S[J_{ee}]_t$ between the pairs ($S\{S[J_{ee}]_t\}_n$) were almost zero (Fig. 2A and B), indicating no plastic changes in J_{ee}. In this K_i range, the system was in a synchronized state characterized by high $E[R_{exc}]_t$ and low $S[R_{exc}]_t$ (Fig. 2C and D). The coupling weights between individual pairs exhibited no fluctuation over time (Fig. 2E, K_i: 0.1; SI Appendix, Movie S1), and the clustered couplings remained unchanged (Fig. 2F, K_i: 0.1).

As K_i increased, $E\{S[J_{ee}]_t\}_n$ also increased, peaking at K_i = 0.7, then decreased, and eventually stabilized around K_i = 1.5 (Fig. 2A). Meanwhile, the $S\{S[J_{ee}]_t\}_n$ continued to increase (Fig. 2B). For K_i values above 1.5, the system entered a desynchronized state characterized by low $E[R_{exc}]_t$ and $S[R_{exc}]_t$ values (Fig. 2C and D). Higher or lower couplings remained stable over time, whereas those of intermediate strength fluctuated (Fig. 2E, K_i: 1.5; SI Appendix, Movie S2). Most clustered couplings at a given time point disappeared over time, leaving only a small subset that remained clustered (Fig. 2F, K_i: 1.5).

In the intermediate range ($0.4 < K_i < 1.5$), the system exhibits a bistable state with high $S[R_{exc}]_t$ (Fig. 2D). Notably, the $S[J_{ee}]_t$ was significantly higher in this bistable state (Fig. 2A). Similar to the desynchronized state ($K_i > 1.5$), the coupling weights of the higher or lower unit pairs were stable, whereas the intermediate-weighted couplings fluctuated more. However, the number of these intermediate fluctuating couplings increased (Fig. 2E and F, K_i: 0.8 and 1.0; SI Appendix, Movies

S3 and S4). Thus, transitions in the dynamic state are accompanied by changes in the coupling weight fluctuations. In particular, the bistable state tended to exhibit larger fluctuations.

Note that Hebbian plasticity affects the dynamic state of the pEI-Kuramoto model (SI Appendix, Fig. S2A), slightly shifting the bifurcation points between the synchronized and bistable states and the bistable and desynchronized states toward larger K_i values. Owing to this effect, a small shift from the eigenvalue-based classification of dynamic states by Kuroki & Muzuseki (2025) was expected. However, the overall trend of the state transition from synchronized to bistable and then to desynchronized remained consistent across different Hebbian learning rates. This behavior is consistent with previous reports on Kuramoto models incorporating cosine-shaped Hebbian plasticity (28, 33). Contrastingly, σ_{Jee} did not affect the dynamic states (SI Appendix, Fig. S2B), which is consistent with the results shown in Fig. 1C.

Strong-weighted couplings are stable while intermediate couplings fluctuated We further investigated coupling weight fluctuations under conditions of slightly weakened inhibition from the desynchronized state, assuming intermediate brain states between alert brain-activated and -deactivated states. We analyzed the individual J_{ee} coupling weights at selected points of K_i (K_i = 0.8, 1.0, and 1.5, red crosses in Fig. 2A–D, except K_i = 0.1). Histograms of $E[J_{ee}]_t$ (mean of J_{ee} over time for each pair of units) and $S[J_{ee}]_t$ also tended to shift toward higher values as K_i decreased (Fig. 3A and B). A scatter plot of $E[J_{ee}]_t$ and $S[J_{ee}]_t$ formed a characteristic "bow-shaped" distribution (Fig. 3C). In this two-dimensional distribution, data points near the minimum and maximum $E[J_{ee}]_t$ values had lower $S[J_{ee}]_t$ values, whereas intermediate $E[J_{ee}]_t$ showed a higher $S[J_{ee}]_t$. This pattern was consistent across all distributions for different K_i values. A similar phenomenon, the stabilization of strong couplings (e.g., synapses with large mushroom-shaped spines), has been observed in brain synapses (38–40).

Furthermore, the $S[J_{ee}]_t$ values tended to increase at intermediate $E[J_{ee}]_t$ values with decreasing K_i (Fig. 3C), suggesting that K_i can regulate the fluctuations in individual J_{ee} plastic couplings. At high K_i values in desynchronized states, the couplings stabilize, whereas at low K_i values in bistable states, the couplings of intermediate weights become unstable. The high J_{ee} coupling remained stable with small fluctuations, even when K_i was low. These dynamics appear to be a mechanism that preserves the coupling of particularly strong pairs and resets pairs of moderate weight, facilitating the reorganization of the network structure (Fig. 2E and 2F).

Factors determining coupling weight properties To determine which parameters determine the individual J_{ee} coupling properties shown in Fig. 3C, we explored the parameters involved in J_{ee} fluctuations. We analyzed the relationship between the individual J_{ee} coupling properties ($E[J_{ee}]_t$ vs. $S[J_{ee}]_t$ distribution shown in Fig. 3C) and the candidate parameters (Fig. 4). The couplings were roughly categorized based on whether $E[J_{ee}]_t$ exceeded 0.018 (high $E[J_{ee}]_t$ group) or not (low $E[J_{ee}]_t$ group) for statistical comparison because the trend reversed around this point.

For the differences in natural frequency (ω_{exc}) of excUnit pairs, smaller natural frequency differences were associated with smaller $S[J_{ee}]_t$ (Fig. 4A and D). Pairs with larger natural frequency differences tended to be in the low-$E[J_{ee}]_t$ group, and $S[J_{ee}]_t$ appeared to increase with increasing natural frequency differences. However, most pairs in the high $E[J_{ee}]_t$ group had relatively small natural frequency differences. The initial phase differences between the pairs were also significant (Fig. 4B and E). In the low $E[J_{ee}]_t$ group, the initial phase differences were uniform, whereas in the high $E[J_{ee}]_t$ group, several pairs exhibited small initial phase differences. Additionally, we examined the effect of the initial coupling weight of J_{ee}, which showed no noticeable bias (Fig. 4C) and followed a normal distribution (Fig. 4F). Considering these results, pairs with small differences in natural frequency and initial phase positions maintained more stable and larger J_{ee} weights (Fig. 4G and H). Contrastingly, the initial J_{ee} weights were not significant.

Theoretical analysis of quasi-steady coupling weight distribution We investigated the theoretical mechanism underlying the numerical simulation results for coupling weights in a quasi-steady state, where values exhibit minimal fluctuation (SI Appendix, Text S1). Although a true static steady weight distribution does not exist in the desynchronized or bistable states due to the non-

constant phases of each oscillator unit, we can consider a quasi-steady weight distribution within the desynchronized condition, where the phase and weight distributions evolve on a sufficiently slow timescale. Under this assumption, the coupling weights do not change as a result of the plastic modulation of Eqs. M11 and M14, which lead to the following relationship (SI Appendix, Eq. S3).

$$J_{ee,kj} = \hat{J}_{ee,kj} + c\exp\left(-\gamma\left|\Delta\theta_{kj}\right|\right) \quad (1).$$

$$c = \frac{\alpha(1-\beta)}{\beta}$$

The first term, $\hat{J}_{ee,kj}$, represents the value of $J_{ee,kj}$ within the normalized distribution of J_{ee} by mean $\hat{\mu}_{Jee}$ and variance $\hat{\sigma}_{Jee}$. This second term is the Hebbian potentiation component, scaled by a ratio between Hebbian and homeostatic plasticity learning rates c. This equation indicates that the weight $J_{ee,kj}$ depends on the distributions of both the overall J_{ee} distribution and the phase differences between unit k and j $\Delta\theta_{kj}$. As this update rule is iterated, the influence of the second $\Delta\theta$-dependent Hebbian term is sequentially incorporated into the J_{ee} distribution. Furthermore, the distribution of $\Delta\theta$ is dependent on the distribution of θ (SI Appendix, Text S1). Therefore, when the weight dynamics are sufficiently slow, the J_{ee} distribution is determined by the phase distribution. Indeed, the characteristics of the J_{ee} distribution appear to be correlated with the synchronization state of the system, which reflects the shape of the phase distribution (Fig 1E, 1F, SI Appendix, Fig S1). Specifically, a uniform phase distribution (desynchronized state) corresponds to a left-skewed, long-tailed J_{ee} distribution. A bimodal phase distribution corresponds to a bimodal J_{ee} distribution. A unimodal phase distribution (synchronized state) corresponds to a right-skewed J_{ee} distribution.

Next, we considered the change in the phase difference for a pair of excUnits $\Delta\theta_{kj}$. Assuming $J_{ee,kj}$ and $\Delta\theta_{kj}$ are constant, the following relationship can be derived from Eqs. M9 and S3 (SI Appendix, Eq. S18):

$$-\Delta\omega + F_{inh} - F_{exc}^{(-kj)} = -2\left\{\hat{J}_{ee,kj} + c\exp\left(-\gamma\left|\Delta\theta_{kj}\right|\right)\right\}\sin\left(\Delta\theta_{kj}\right) \quad (2).$$

$\Delta\omega$ is natural frequency difference between unit k and j, F_{inh} is interaction strength from the inhUnits, and $F_{exc}^{(-kj)}$ is interaction strength from the excUnits except unit k and j. The right-hand side of this equation represents the interaction strength between the unit k and j, while the left-hand side represents the net forces of the other factors. A stable fixed point for $\Delta\theta_{kj}$ exists where the functions for the left and right-hand sides intersect (SI Appendix, Fig. S3). On the right-hand side, the attractive force is driven by both the homeostatic set-point, $\hat{J}_{ee,kj}$, and the Hebbian potentiation term. Near $\Delta\theta\approx0$, the Hebbian effect is strong, leading to a large attractive force. As the phase difference $|\Delta\theta|$ increases, this Hebbian potentiation weakens and the coupling weight relative position within the J_{ee} distribution falls to a lower, causing reduction of the overall attractive force. The left-hand side represents the net external drive on the pair. This drive is composed of the natural frequency difference $\Delta\omega$ and the R_{exc} and R_{inh}-dependent term $F_{inh} - F_{exc}^{(-kj)}$, whose direction can be either attractive or repulsive depending on the phase configuration of the system. (SI Appendix, Text S1). While the influence of F_{inh} and $F_{exc}^{(-kj)}$ is limited in a desynchronized state where R_{exc} and R_{inh} are near zero, their impact becomes significant in the bistable state, where these order parameters fluctuate periodically. Sufficient fluctuation in these forces can overcome the attractive force represented by the right-hand side, causing the stable fixed point to either disappear or be significantly displaced. This leads to large fluctuations in the phase difference between the unit pair.

Cyclic modulation of inhibition Finally, we varied K_i to mimic the sleep-wake cycle (7). J_{ee} fluctuated (Fig. 5A, SI Appendix, Movie S5) according to the modulation of K_i (Fig. 5B, top panel). R_{exc} alternated between the desynchronized and bistable states (Fig. 5B, middle), and $E\{S[J_{ee}]_t\}_n$ changed accordingly (Fig. 5B, bottom). When K_i was high, the system was in a desynchronized state, and $E\{S[J_{ee}]_t\}_n$ was small. Conversely, when K_i was low, the system exhibits a bistable state and $E\{S[J_{ee}]_t\}_n$ increases. These dynamics can be considered as modeling how the circuit structure

is stabilized during the brain-activated state and destabilized during the brain-deactivated state, thereby promoting circuit reorganization.

Discussion

In this study, we extended the previously developed EI-Kuramoto model by incorporating Hebbian and homeostatic plasticity to establish the pEI-Kuramoto model and analyze its dynamics. We propose that this model represents a continuous transition between the stabilization and reorganization of network structures, modulated by the desynchronized-bistable state cycle through inhibition (see Figs 2–5). This study introduces a possible mechanism for preserving strong couplings and reorganizing network structures during brain-deactivated states, as viewed through the dynamics of collective oscillators.

Potential mechanism for network reorganization Preserving robust couplings while randomizing weaker ones simplifies the network by rendering them sparse. The choice of plasticity parameters, which yield a long-tailed coupling weight distribution similar to that observed in the brain (Fig. 1E and F) and mirror brain dynamics during the brain-deactivated state (9–12), appears to facilitate network sparsification. The selective preservation of strong synaptic connections is also frequently observed in the brain (38–40) and is understood through molecular mechanisms, including the dynamics of NMDA receptors (5, 41) and actin filaments (42). Our findings introduce a potential mechanism for sustaining strong coupling when viewed from another aspect of the dynamic system of collective oscillators. In addition, at the system level, only a few populations of neuronal activity are stable, while others drift even in familiar environments (43–45). This process aligns with the pruning method in artificial neural networks, which facilitates knowledge generalization (46, 47). This pruning-like mechanism is particularly relevant when synaptic downregulation is dominant during brain-deactivated states (5, 41), as fluctuations in couplings can lead to the weakening and initialization of the couplings. Furthermore, fluctuations in network connectivity can promote both orderly and random network reorganization. In our model, bistable states under low inhibition conditions promoted fluctuating coupling weights between excUnits. As the inhibition decreases, the process transitions from structured coupling weight changes governed by the Hebbian rule to nearly random changes driven by the large phase fluctuations of the units (see Supplementary Videos 2–5). It has also been proposed that the brain enhances neuronal circuit reorganization during brain-deactivated state (3, 4). Combined with unknown mechanisms to evaluate and stabilize reorganized circuits (48) such as dopaminergic signaling during non-REM sleep (49), we may approach how new creative ideas or inexperienced problem-solving methods are generated.

Dynamics of pEI-Kuramoto model From the stability analysis of the phase difference between excUnit pair (Eq. 2), the characteristic bow-shaped relationship between the mean ($E[J_{ee}]_t$) and standard deviation ($S[J_{ee}]_t$) of coupling weights (Fig. 3C) can be explained. Pairs of strong couplings maintain a small and stable phase difference ($\Delta\theta \approx 0$). This ensures that the Hebbian potentiation term, $c\exp(-\gamma|\Delta\theta_{kj}|)$, and $\hat{J}_{ee,kj}$, associated with relative position in the J_{ee} distribution, remains consistently high. Consequently, these synapses sustain a high $E[J_{ee}]_t$ with very small fluctuations, resulting in a low $S[J_{ee}]_t$. These pairs form the top-left end of the bow in Fig 3C. On the other side in the plot, the phases of unit pairs with very weak couplings evolve almost independently. The Hebbian potentiation effect is negligible, and their synaptic weights remain at a low baseline value determined by homeostatic pressures. As a result, $S[J_{ee}]_t$ at a particular time window depends primarily on the natural frequency difference $\Delta\omega$. The largest $S[J_{ee}]_t$ is found in pairs with intermediate coupling strength. For these couplings, the synchronizing force is in close competition with the desynchronizing drives from their natural frequency difference $\Delta\omega$. The system is critically poised: small fluctuations in $\Delta\theta$ can tip the balance between Hebbian potentiation and homeostatic depression, causing the direction of weight change to reverse frequently. This instability, where the fixed point for $\Delta\theta$ may appear and disappear intermittently, drives large fluctuations in the coupling weight J_{ee}. This mechanism produces a high variance at intermediate mean weights, forming the arch of the bow. From a

dynamics perspective, this mechanism may explain a characteristic feature of biological synapses: larger synapses are more stable than smaller ones (38–40).

The fluctuation of J_{ee} when K_i is low can be attributed to the system dynamics becoming bistable, where the system alternates between synchronization and desynchronization. It causes fluctuations in the phase distribution, which is the primary factor driving the changes in J_{ee}. Furthermore, in this state, the periodic fluctuation of the order parameters R_{exc}, R_{inh} constant changes in the interaction term, $F_{inh} - F_{exc}^{(-kj)}$ (Eq. 2). This dynamic instability also strongly perturbs the phase differences Δθ of moderately coupled pairs more.

The Eq. 2 suggests that unit pairs with small initial frequency Δω and phase differences Δθ are more robust and more likely to return to a stable, synchronized state even after large perturbations. This provides an explanation for the results shown in Figure 4. This finding resonates with observations in the brain, where neurons that exhibit synchronized firing prior to learning (analogous to a small Δθ) are more likely to be grouped into the same assembly during learning (50–52). However, it remains unclear whether these neurons also share similar intrinsic firing frequencies, which would correspond to a small Δω in our model. Although the effective interaction function in our simulation setting (Fig. 1F, magenta circle), designed to approximate biological synaptic distributions (12, 34, 35), deviates slightly from a pure sine wave by providing a stronger restoring force near the stable point (Fig. S3), the enhancement of interaction strength near Δθ=0 by the Hebbian effect is limited. Thus, it appears that this property stems primarily from the underlying sinusoidal nature of the coupling, rather than from the modifications introduced by plasticity.

The quasi-steady J_{ee} distribution is determined by the phase difference distribution (Fig 1E, 1F, and SI Appendix, Fig S1), as it is a transformation of the Δθ distribution via the Hebbian function (Eq. 1). In this study, the exponential rule $c\exp\left(-\gamma\left|\Delta\theta_{kj}\right|\right)$ transforms the uniform phase difference distribution into a hyperbolic-like weight distribution, with a probability density proportional to $1/J_{ee}$ (Appendix, Text S1). This framework suggests that, by modifying the Hebbian function, it is possible to generate the J_{ee} distribution into an arbitrary form, such as a log-normal distribution that observed in the brain (12, 34, 35).

Limitations While the Kuramoto model provides foundational insights, it is considerably simpler than actual neuronal behavior and has certain limitations. First, our model simplifies neuronal interactions to mere attractive and repulsive forces, overlooking the pulse-like nature, interaction delay, and intricate coupling relationships of real neurons (53). Second, the model underrepresents the complexity of neuroplasticity, such as the influence of neurotransmitters and internal conditions (54), plasticity in inhibitory neurons (55, 56), and short-term plasticity including adaptation (57). Lastly, the model does not distinguish between brain states, such as full wakefulness, non-REM sleep, and REM sleep, which are believed to play unique roles in learning and neural reorganization (3, 4). Addressing these limitations is essential for a more accurate and comprehensive understanding of the neural dynamics and plasticity.

Future directions Future research can consider multiple directions to expand the system further. In this study, we observed a behavior in which strong couplings were retained and intermediate couplings were randomly perturbed at low inhibition. Creativity may require a mechanism for evaluating and stabilizing randomly reorganized circuits (48, 58). This mechanism is not yet fully understood; however, dopamine activity during rest (49) may be a key factor. Another important question is how changes in overall synchrony during sleep affect the interactions between functionally distinct networks, such as the hippocampus and cerebral cortex. Exploring the influence of synchrony transitions on interregional plasticity could shed light on how memory traces originally stored in the hippocampus gradually become integrated or transferred to cortical areas (59). Moreover, our model did not specifically consider the dimensionality of information, but understanding how the brain represents and selects multidimensional information is crucial for cognition (60). We must consider the biases, interactions, and plasticity rules required to represent and select multidimensional information from the external world. Clarifying these

mechanisms will contribute to a deeper understanding of how neural circuits are reorganized to support abstraction and creativity.

Materials and Methods

pEI-Kuramoto model The original Kuramoto model (13, 14, 61) is expressed as:

$$\frac{d\theta_j(t)}{dt} = \omega_j + \frac{K}{N}\sum_{k}^{N} \sin\left(\theta_k(t) - \theta_j(t)\right) \quad \text{(M1)},$$

where $\theta_j(t)$ is the phase of unit j at time t, ω_j is the natural frequency of unit j following a probability distribution $g(\omega)$, N is the number of units, and K is the interaction strength among the oscillation units. In the original Kuramoto model, K is constantly and uniformly applied to all unit pairs. The order parameter R and the mean phase ψ are then calculated from the mean vector of the oscillators as:

$$Re^{i\psi} = \frac{1}{N}\sum_{j}^{N} e^{i\theta_j} \quad \text{(M2)},$$

where i denotes an imaginary unit. Given Euler's formula and Eq (2),

$$\frac{1}{N}\sum_{k}^{N} \sin(\theta_k - \theta_j) = \frac{1}{N}\sum_{k}^{N} \mathrm{Im}\left[e^{i\theta_k}e^{-i\theta_j}\right] = \mathrm{Im}\left[Re^{i\psi}e^{-i\theta_j}\right] = R\sin(\psi - \theta_j) \quad \text{(M3)}.$$

Considering, Eq (3), Eq (1) becomes

$$\frac{d\theta_j}{dt} = \omega_j + KR\sin(\psi - \theta_j) \quad \text{(M4)}.$$

In our previous EI-Kuramoto model (16), the oscillation units were categorized into two groups: excitatory and inhibitory units, referred to as excUnits and inhUnits, respectively. Employing these terms clarified that the units in the model represented excitatory and inhibitory factors, distinguishing them from actual neurons or synapses. The interaction strength of the sine wave functions with zero phase lag is characterized by purely attractive interactions in excUnits and purely repulsive interactions in inhUnits. Hence, the terms "excitatory" and "inhibitory" are used interchangeably with "attractive" and "repulsive," respectively. The interaction strength K is divided into four quantifiable parameters: K_{ee} (attractive strength between excUnits), K_{ii} (repulsive strength between inhUnits), K_{ei} (attractive strength from excUnits to inhUnits), and K_{ie} (repulsive strength from inhUnits to excUnits). K_{ee}, K_{ii}, K_{ei}, and K_{ie} are distinct positive real numbers that are uniformly applicable across all the unit pairs. Consequently, Eq (M4) becomes:

$$\frac{d\theta_{j,exc}}{dt} = \omega_{j,exc} + K_{ee}R_{exc}\sin(\psi_{exc} - \theta_{j,exc}) - K_{ie}R_{inh}\sin(\psi_{inh} - \theta_{j,exc}) \quad \text{(M5)}$$

for excUnits, and

$$\frac{d\theta_{j,inh}}{dt} = \omega_{j,inh} + K_{ei}R_{exc}\sin(\psi_{exc} - \theta_{j,inh}) - K_{ii}R_{inh}\sin(\psi_{inh} - \theta_{j,inh}) \quad \text{(M6)}$$

for inhibUnits, where exc and inh represent the parameters for excUnits and inhUnits, respectively. The order parameter and mean phase of each excUnit and inhUnit are

$$R_{exc}e^{i\psi_{exc}} = \frac{1}{N_{exc}}\sum_{j}^{N_{exc}} e^{i\theta_{j,exc}} \quad \text{(M7)}$$

and

$$R_{inh}e^{i\psi_{inh}} = \frac{1}{N_{inh}}\sum_{j}^{N_{inh}} e^{i\theta_{j,inh}} \quad \text{(M8)}.$$

In the present study, we developed a pEI-Kuramoto model (Fig. 1A). A pivotal modification of our previous EI-Kuramoto model is that the constant and uniform interaction strength value K_{ee} is replaced with the heterogeneous and plastic coupling weight (interaction strength of an individual unit pair) matrix J_{ee}. The initial distribution of J_{ee} follows the Gaussian distribution $g(J_{ee}) \sim \mathcal{N}(\mu_{Jee}/N_{exc}, (\sigma_{Jee}/N_{exc})^2)$, where μ_{Jee} and σ_{Jee} are the mean and standard deviation of the J_{ee} distribution, respectively. These were scaled with the inverse of N_{exc} to adjust for the system size. The other interaction strengths, K_{ii}, K_{ei}, and K_{ie}, were uniform and consistently applicable across all units. Eq (M5) becomes

$$\frac{d\theta_{j,exc}}{dt} = \omega_{j,exc} + \sum_{k}^{N_{exc}} J_{ee,kj} \sin\left(\theta_{k,exc} - \theta_{j,exc}\right) - K_{ie} R_{inh} \sin\left(\psi_{inh} - \theta_{j,exc}\right) \quad \text{(M9)}.$$

$J_{ee,kj}$ is the coupling weight between the excUnits k (pre) and j (post).

Given the rotational symmetry, when the mean natural frequencies of excUnits and inhUnits are equal, $\bar{\omega} = \bar{\omega}_{exc} = \bar{\omega}_{inh}$, the mean natural frequencies can be set to 0 rad/s. This is equivalent to rotating a coordinate by the mean natural frequency $\bar{\omega}$ (61). For all simulations in this study, $N_{exc} = 80$, $N_{inh} = 20$, total simulation duration $T = 50$ s, time step $dt = 0.01$ s, $g(\omega)$ of both excUnits and inhUnits followed Gaussian distribution $g(\omega) \sim \mathcal{N}(0, 0.01)$ for both excUnits and inhUnits. The range of time to evaluate the mean of the order parameters R_{exc} and R_{inh} was from T/2 to T to exclude initial fluctuations. In Fig. 2–5, K_{ii} and K_{ie} are integrated with the same parameter K_i to simplify the simulation.

$$K_i = K_{ie} = K_{ii} \quad \text{(M10)}.$$

At each time step, the J_{ee} values were first modulated by Hebbian potentiation and then rescaled using homeostatic regularization rules. The Hebbian potentiation plasticity is implemented as an exponential function:

$$\frac{dJ_{ee,kj}}{dt} = \alpha \exp\left(-\gamma \left|\Delta\theta_{kj}\right|\right) \quad (11).$$

$$J_{Hebb} \leftarrow J_{ee,kj} + \alpha \exp\left(-\gamma \left|\Delta\theta_{kj}\right|\right) \quad \text{(M11)}.$$

α is a learning rate for the Hebbian plasticity. Note that α should scale proportionally with an inverse of N_{exc} as $\alpha \propto 1/N_{exc}$ to maintain consistency across different system sizes. γ determines a sharpness exponential decay from the peak. $\Delta\theta_{kj}$ is the phase difference between excUnit k and j

$$\Delta\theta_{kj} = \theta_{k,exc} - \theta_{j,exc} \left(-\pi \leq \Delta\theta_{kj} < \pi\right) \quad \text{(M12)}.$$

The implementation of Hebbian plasticity with a cosine function (SI Appendix, Fig. S1) is defined

$$\frac{dJ_{ee,kj}}{dt} = \frac{\alpha}{2}\{\cos\left(\Delta\theta_{kj}\right) + 1\} \quad (13).$$

$$J_{Hebb} \leftarrow J_{ee,kj} + \frac{\alpha}{2}\{\cos\left(\Delta\theta_{kj}\right) + 1\} \quad \text{(M13)}.$$

In any Hebbian learning rule in this paper, $dJ_{ee,kj}/dt = dJ_{ee,jk}/dt$ holds due to the symmetry with respect to the sign of $\Delta\theta_{kj}$.

After the Hebbian modulations, J_{ee} was rescaled with the homeostatic regularization plasticity rule to prevent overpotentiation. Plasticity was implemented as follows:

$$\hat{J}_{ee,kj} = \frac{\hat{\sigma}_{Jee}}{S[J_{ee}]_n}\left(J_{ee,kj} - E[J_{ee}]_n\right) + \hat{\mu}_{Jee}$$

$$J_{ee,kj} \leftarrow \beta \hat{J}_{ee,kj} + (1-\beta) J_{ee,kj} \quad (14).$$

$$\hat{J}_{ee,kj} = \frac{\hat{\sigma}_{Jee}}{S[J_{Hebb}]_n}\left(J_{Hebb} - E[J_{Hebb}]_n\right) + \hat{\mu}_{Jee}$$

$$J_{ee,kj} \leftarrow \beta \hat{J}_{Hebb} + (1-\beta) J_{Hebb} \quad \text{(M14)}.$$

$J_{ee,kj}$ is scaled adjusting to initial μ_{Jee} and σ_{Jee} settings, $\hat{\mu}_{Jee} = \mu_{Jee}/N_{exc}$, $\hat{\sigma}_{Jee} = \sigma_{Jee}/N_{exc}$. $E[J_{ee}]_n$ and $S[J_{ee}]_n$ are the calculated mean and standard deviation of the J_{ee} distribution among the units

at every time point immediately after Hebbian modification, respectively. β is a learning rate for the regularization plasticity. This process rescales the J_{ee} distribution toward distribution with mean $\hat{\mu}_{Jee}$ and standard deviation $\hat{\sigma}_{Jee}$.

Cyclic inhibitory modulation In Fig. 5, K_i is modulated as a sine function

$$K_i = A_s \sin(\omega_s t) + C_s \quad \text{(M15)},$$

where A_s (= 0.32), ω_s (= 0.004π), and C_s (= 1.4) are the amplitude, frequency, and baseline constant for the sine modulation, respectively. The other parameters for interaction strengths are held constant to simplify the simulation; μ_{Jee} = 1, σ_{Jee} = 0.1, and K_{ei} = 3.

Statistics $E[\cdot]_t$ (also $E\{\cdot\}_t$) and $S[\cdot]_t$ are the mean and the standard deviation over time, respectively, where t indicates the number of time points. $E[\cdot]_n$ and $S[\cdot]_n$ are the mean and the standard deviation among unit pairs, respectively, where n indicates the number of unit pairs. Where · represents a certain variable. For Fig. 5B lower panel, the time window (±15 sec from the time point) was set.

Descriptive statistics (mean, standard deviation, kurtosis, and skewness) and statistical tests were performed using Python Numpy and Scipy libraries. The Dip test (36) was performed using the Python Diptest Library (https://github.com/RUrlus/diptest). The dip value is the maximum distance between the actual data distribution and the fitting result of the monomodal Gaussian distribution. If the data distribution is close to a monomodal Gaussian distribution, the dip value is low. If is bimodal, then its value is high. Hierarchical clustering was performed using the linkage function of the Python Scipy library.

Code Availability Statement The scripts for this study can be found at Google Colaboratory: https://colab.research.google.com/drive/1v8JF97G9YdwUOh_Wuh9i_TvuGa42fLAu?usp=sharing

Acknowledgments

We would like to thank Susumu Setogawa for their insightful contributions to the discussion. This study was supported by JSPS KAKENHI [grant 24K18243 to S.K.; grant 23H02788 to K.M.] and the Takeda Science Foundation [to K.M.]. The funding sources had no involvement in the study design, data collection, interpretation, or the decision to submit this paper for publication.

References

1. G. Wallas, *The art of thought* (Jonathan Cape, 1926).
2. J. G. Jenkins, K. M. Dallenbach, Obliviscence during sleep and waking. *Am. J. Psychol.* **35**, 605 (1924).
3. N. Landmann, et al., The reorganisation of memory during sleep. *Sleep Med. Rev*. **18,** 531–541 (2014).
4. P. A. Lewis, G. Knoblich, G. Poe, How memory replay in sleep boosts creative problem-solving. *Trends Cogn. Sci.* **22**, 491–503 (2018).
5. H. Norimoto, et al., Hippocampal ripples down-regulate synapses. *Science* **359**, 1524–1527 (2018).
6. A. Goto, et al., Stepwise synaptic plasticity events drive the early phase of memory consolidation. *Science* **374,** 857–863 (2021).
7. K. D. Harris, A. Thiele, Cortical state and attention. *Nat. Rev. Neurosci*. **12**, 509–523 (2011).
8. M. Steriade, R. R. Llinás, The functional states of the thalamus and the associated neuronal interplay. *Physiol. Rev*. **68**, 649–742 (1988).
9. B. Haider, M. Häusser, M. Carandini, Inhibition dominates sensory responses in the awake cortex. *Nature* **493,** 97–100 (2013).

10. H. Miyawaki, K. Diba, Regulation of hippocampal firing by network oscillations during sleep. *Curr. Biol*. **26**, 893–902 (2016).
11. H. Alfonsa, et al., Intracellular chloride regulation mediates local sleep pressure in the cortex. *Nat. Neurosci*. **26**, 64–78 (2022).
12. K. Mizuseki, G. Buzsáki, Preconfigured, skewed distribution of firing rates in the hippocampus and entorhinal cortex. *Cell Rep*. **4**, 1010–1021 (2013).
13. Y. Kuramoto, Chemical oscillations, waves, and turbulence (Springer, 1984).
14. Y. Kuramoto, Self-entrainment of a population of coupled non-linear oscillators in International Symposium on Mathematical Problems in Theoretical Physics (Springer, 1975), pp. 420–422.
15. E. Montbrió, D. Pazó, Kuramoto model for excitation-inhibition-based oscillations. *Phys. Rev. Lett.* **120,** 244101 (2018).
16. S. Kuroki, K. Mizuseki, Excitation-inhibition balance controls synchronization in a simple model of coupled phase oscillators. *Neural Comput*. **37**, 1353–1372 (2025).
17. D. O. Hebb, The organization of behavior; a neuropsychological theory (Wiley, 1949).
18. G. G. Turrigiano, The self-tuning neuron: synaptic scaling of excitatory synapses. ***Cell*** **135**, 422–435 (2008).
19. T. Toyoizumi, M. Kaneko, M. P. Stryker, K. D. Miller, Modeling the dynamic interaction of Hebbian and homeostatic plasticity. *Neuron* **84**, 497–510 (2014).
20. S. Kim, D. Jung, S. Royer, Place cell maps slowly develop via competitive learning and conjunctive coding in the dentate gyrus. *Nat. Commun*. **11**, 4550 (2020).
21. S. Benas, X. Fernandez, E. Kropff, Modeled grid cells aligned by a flexible attractor. *eLife* (2024).
22. S. N. Weber, H. Sprekeler, Learning place cells, grid cells and invariances with excitatory and inhibitory plasticity. *eLife* **7**, e34560 (2018).
23. T. Aoki, T. Aoyagi, Co-evolution of phases and connection strengths in a network of phase oscillators. *Phys. Rev. Lett.* **102**, 034101 (2009).
24. J. C. Bronski, et al., The stability of fixed points for a Kuramoto model with Hebbian interactions. *Chaos* **27**, 053110 (2017).
25. J. Fialkowski, et al., Heterogeneous nucleation in finite-size adaptive dynamical networks. *Phys. Rev. Lett.* **130**, 067402 (2023).
26. S. Y. Ha, J. Lee, Z. Li, J. Park, Emergent dynamics of Kuramoto oscillators with adaptive couplings: Conservation law and fast learning. *SIAM J. Appl. Dyn. Syst*. **17**, 1560–1588 (2018).
27. S. Y. Ha, S. E. Noh, J. Park, Synchronization of Kuramoto oscillators with adaptive couplings. *SIAM J. Appl. Dyn. Syst.* **15**, 162–194 (2016).
28. R. K. Niyogi, L. Q. English, Learning-rate-dependent clustering and self-development in a network of coupled phase oscillators. *Phys. Rev. E Stat. Nonlin. Soft Matter Phys.* **80**, 066213 (2009).
29. J. Park, D. Poyato, J. Soler, Filippov trajectories and clustering in the Kuramoto model with singular couplings. *J. Eur. Math. Soc.* **23**, 3193–3278 (2021).
30. C. B. Picallo, H. Riecke, Adaptive oscillator networks with conserved overall coupling: Sequential firing and near-synchronized states. *Phys. Rev. E Stat. Nonlin. Soft Matter Phys.* **83**, 036206 (2011).
31. D. Poyato, Filippov flows and mean-field limits in the kinetic singular Kuramoto model. *arXiv [math.AP]* (2019).
32. Q. Ren, J. Zhao, Adaptive coupling and enhanced synchronization in coupled phase oscillators. *Phys. Rev. E Stat. Nonlin. Soft Matter Phys.* **76**, 016207 (2007).
33. P. Seliger, S. C. Young, L. S. Tsimring, Plasticity and learning in a network of coupled phase oscillators. *Phys. Rev. E Stat. Nonlin. Soft Matter Phys*. **65**, 041906 (2002).
34. G. Buzsáki, K. Mizuseki, The log-dynamic brain: how skewed distributions affect network operations. *Nat. Rev. Neurosci.* **15**, 264–278 (2014).
35. M. Iwase, K. Diba, E. Pastalkova, K. Mizuseki, Dynamics of spike transmission and suppression between principal cells and interneurons in the hippocampus and entorhinal cortex. *Hippocampus* **34**, 393–421 (2024).

36. J. A. Hartigan, P. M. Hartigan, The dip test of unimodality. *Ann. Stat.* **13**, 70–84 (1985).
37. A. C. Nobre, S. Kastner, Eds., The Oxford Handbook of Attention (Oxford University Press, 2014).
38. A. J. G. D. Holtmaat, et al., Transient and persistent dendritic spines in the neocortex in vivo. *Neuron* **45**, 279–291 (2005).
39. M. Matsuzaki, N. Honkura, G. C. R. Ellis-Davies, H. Kasai, Structural basis of long-term potentiation in single dendritic spines. *Nature* **429**, 761–766 (2004).
40. J. Grutzendler, N. Kasthuri, W.-B. Gan, Long-term dendritic spine stability in the adult cortex. *Nature* **420**, 812–816 (2002).
41. G. Tononi, C. Cirelli, Sleep and synaptic down-selection. *Eur. J. Neurosci.* **51**, 413–421 (2020).
42. H. Kasai, et al., Learning rules and persistence of dendritic spines. *Eur. J. Neurosci*. **32**, 241–249 (2010).
43. L. Bollmann, P. Baracskay, F. Stella, J. Csicsvari, Sleep stages antagonistically modulate reactivation drift. *Neuron* **113,** 1446-1459.e6 (2025).
44. S. P. Vaidya, G. Li, R. A. Chitwood, Y. Li, J. C. Magee, Formation of an expanding memory representation in the hippocampus. *Nature Neurosci.*, in press.
45. Y. Ziv, et al., Long-term dynamics of CA1 hippocampal place codes. *Nat. Neurosci.* **16**, 264–266 (2013).
46. D. T. Campbell, Blind variation and selective retention in creative thought as in other knowledge processes. *Psychol. Rev.* **67**, 380–400 (1960).
47. S. N. Gomperts, F. Kloosterman, M. A. Wilson, VTA neurons coordinate with the hippocampal reactivation of spatial experience. *eLife* **4**, e05360 (2015).
48. E. M. Izhikevich, Dynamical systems in neuroscience: The geometry of excitability and bursting (MIT Press, 2010).
49. Z. Brzosko, S. B. Mierau, O. Paulsen, Neuromodulation of spike-timing-dependent plasticity: Past, present, and future. *Neuron* **103**, 563–581 (2019).
50. Y. K. Wu, C. Miehl, J. Gjorgjieva, Regulation of circuit organization and function through inhibitory synaptic plasticity. *Trends Neurosci*. **45,** 884–898 (2022).
51. C. Q. Chiu, A. Barberis, M. J. Higley, Preserving the balance: diverse forms of long-term GABAergic synaptic plasticity. *Nat. Rev. Neurosci*. **20**, 272–281 (2019).
52. D. M. Blitz, K. A. Foster, W. G. Regehr, Short-term synaptic plasticity: a comparison of two synapses. *Nat. Rev. Neurosci*. **5,** 630–640 (2004).
53. R. E. Beaty, M. Benedek, P. J. Silvia, D. L. Schacter, Creative cognition and brain network dynamics. *Trends Cogn. Sci.* **20**, 87–95 (2016).
54. J. G. Klinzing, N. Niethard, J. Born, Mechanisms of systems memory consolidation during sleep. *Nat. Neurosci*. **22**, 1598–1610 (2019).
55. O. Barak, Recurrent neural networks as versatile tools of neuroscience research. *Curr. Opin. Neurobiol.* **46**, 1–6 (2017).
56. J. A. Acebrón, L. L. Bonilla, C. J. Pérez Vicente, F. Ritort, R. Spigler, The Kuramoto model: A simple paradigm for synchronization phenomena. *Rev. Mod. Phys.* **77**, 137–185 (2005).

1. J. G. Jenkins, K. M. Dallenbach, Obliviscence during sleep and waking. *Am. J. Psychol.* **35**, 605 (1924).
2. G. Wallas, *The art of thought* (Jonathan Cape, 1926).
3. N. Landmann, *et al.*, The reorganisation of memory during sleep. *Sleep Med. Rev.* **18**, 531–541 (2014).
4. P. A. Lewis, G. Knoblich, G. Poe, How memory replay in sleep boosts creative problem-solving. *Trends Cogn. Sci.* **22**, 491–503 (2018).
5. H. Norimoto, *et al.*, Hippocampal ripples down-regulate synapses. *Science* **359**, 1524–1527 (2018).
6. A. Goto, *et al.*, Stepwise synaptic plasticity events drive the early phase of memory consolidation. *Science* **374**, 857–863 (2021).

7. K. D. Harris, A. Thiele, Cortical state and attention. *Nat. Rev. Neurosci.* **12**, 509–523 (2011).
8. M. Steriade, R. R. Llinás, The functional states of the thalamus and the associated neuronal interplay. *Physiol. Rev.* **68**, 649–742 (1988).
9. B. Haider, M. Häusser, M. Carandini, Inhibition dominates sensory responses in the awake cortex. *Nature* **493**, 97–100 (2013).
10. H. Miyawaki, K. Diba, Regulation of hippocampal firing by network oscillations during sleep. *Curr. Biol.* **26**, 893–902 (2016).
11. H. Alfonsa, *et al.*, Intracellular chloride regulation mediates local sleep pressure in the cortex. *Nat. Neurosci.* **26**, 64–78 (2022).
12. K. Mizuseki, G. Buzsáki, Preconfigured, skewed distribution of firing rates in the hippocampus and entorhinal cortex. *Cell Rep.* **4**, 1010–1021 (2013).
13. Y. Kuramoto, *Chemical oscillations, waves, and turbulence* (Springer, 1984).
14. Y. Kuramoto, Self-entrainment of a population of coupled non-linear oscillators in *International Symposium on Mathematical Problems in Theoretical Physics*, (Springer, 1975), pp. 420–422.
15. E. Montbrió, D. Pazó, Kuramoto model for excitation-inhibition-based oscillations. *Phys. Rev. Lett.* **120**, 244101 (2018).
16. S. Kuroki, K. Mizuseki, Excitation-inhibition balance controls synchronization in a simple model of coupled phase oscillators. *Neural Comput.* **37**, 1353–1372 (2025).
17. D. O. Hebb, *The organization of behavior; a neuropsychological theory* (Wiley, 1949).
18. G. G. Turrigiano, The self-tuning neuron: synaptic scaling of excitatory synapses. *Cell* **135**, 422–435 (2008).
19. T. Toyoizumi, M. Kaneko, M. P. Stryker, K. D. Miller, Modeling the dynamic interaction of Hebbian and homeostatic plasticity. *Neuron* **84**, 497–510 (2014).
20. S. Kim, D. Jung, S. Royer, Place cell maps slowly develop via competitive learning and conjunctive coding in the dentate gyrus. *Nat. Commun.* **11**, 4550 (2020).
21. S. Benas, X. Fernandez, E. Kropff, Modeled grid cells aligned by a flexible attractor. *eLife* (2024).
22. S. N. Weber, H. Sprekeler, Learning place cells, grid cells and invariances with excitatory and inhibitory plasticity. *Elife* **7**, e34560 (2018).
23. T. Aoki, T. Aoyagi, Co-evolution of phases and connection strengths in a network of phase oscillators. *Phys. Rev. Lett.* **102**, 034101 (2009).
24. J. C. Bronski, *et al.*, The stability of fixed points for a Kuramoto model with Hebbian interactions. *Chaos* **27**, 053110 (2017).
25. J. Fialkowski, *et al.*, Heterogeneous nucleation in finite-size adaptive dynamical networks. *Phys. Rev. Lett.* **130**, 067402 (2023).
26. S. Y. Ha, J. Lee, Z. Li, J. Park, Emergent dynamics of Kuramoto oscillators with adaptive couplings: Conservation law and fast learning. *SIAM J. Appl. Dyn. Syst.* **17**, 1560–1588 (2018).
27. S. Y. Ha, S. E. Noh, J. Park, Synchronization of Kuramoto oscillators with adaptive couplings. *SIAM J. Appl. Dyn. Syst.* **15**, 162–194 (2016).
28. R. K. Niyogi, L. Q. English, Learning-rate-dependent clustering and self-development in a network of coupled phase oscillators. *Phys. Rev. E Stat. Nonlin. Soft Matter Phys.* **80**, 066213 (2009).
29. J. Park, D. Poyato, J. Soler, Filippov trajectories and clustering in the Kuramoto model with singular couplings. *J. Eur. Math. Soc.* **23**, 3193–3278 (2021).
30. C. B. Picallo, H. Riecke, Adaptive oscillator networks with conserved overall coupling: Sequential firing and near-synchronized states. *Phys. Rev. E Stat. Nonlin. Soft Matter Phys.* **83**, 036206 (2011).
31. D. Poyato, Filippov flows and mean-field limits in the kinetic singular Kuramoto model. *arXiv [math.AP]* (2019).
32. Q. Ren, J. Zhao, Adaptive coupling and enhanced synchronization in coupled phase oscillators. *Phys. Rev. E Stat. Nonlin. Soft Matter Phys.* **76**, 016207 (2007).

33. P. Seliger, S. C. Young, L. S. Tsimring, Plasticity and learning in a network of coupled phase oscillators. *Phys. Rev. E Stat. Nonlin. Soft Matter Phys.* **65**, 041906 (2002).
34. G. Buzsáki, K. Mizuseki, The log-dynamic brain: how skewed distributions affect network operations. *Nat. Rev. Neurosci.* **15**, 264–278 (2014).
35. M. Iwase, K. Diba, E. Pastalkova, K. Mizuseki, Dynamics of spike transmission and suppression between principal cells and interneurons in the hippocampus and entorhinal cortex. *Hippocampus* **34**, 393–421 (2024).
36. J. A. Hartigan, P. M. Hartigan, The dip test of unimodality. *Ann. Stat.* **13**, 70–84 (1985).
37. A. C. Nobre, S. Kastner, Eds., *The Oxford Handbook of Attention* (Oxford University Press, 2014).
38. A. J. G. D. Holtmaat, *et al.*, Transient and persistent dendritic spines in the neocortex in vivo. *Neuron* **45**, 279–291 (2005).
39. M. Matsuzaki, N. Honkura, G. C. R. Ellis-Davies, H. Kasai, Structural basis of long-term potentiation in single dendritic spines. *Nature* **429**, 761–766 (2004).
40. J. Grutzendler, N. Kasthuri, W.-B. Gan, Long-term dendritic spine stability in the adult cortex. *Nature* **420**, 812–816 (2002).
41. G. Tononi, C. Cirelli, Sleep and synaptic down-selection. *Eur. J. Neurosci.* **51**, 413–421 (2020).
42. H. Kasai, *et al.*, Learning rules and persistence of dendritic spines. *Eur. J. Neurosci.* **32**, 241–249 (2010).
43. L. Bollmann, P. Baracskay, F. Stella, J. Csicsvari, Sleep stages antagonistically modulate reactivation drift. *Neuron* **113**, 1446-1459.e6 (2025).
44. S. P. Vaidya, G. Li, R. A. Chitwood, Y. Li, J. C. Magee, Formation of an expanding memory representation in the hippocampus. *Nature Neuroscience* 1–9 (2025).
45. Y. Ziv, *et al.*, Long-term dynamics of CA1 hippocampal place codes. *Nat. Neurosci.* **16**, 264–266 (2013).
46. B. Bartoldson, A. Morcos, A. Barbu, G. Erlebacher, The generalization-stability tradeoff in neural network pruning in *Advances in Neural Information Processing Systems*, H. Larochelle, M. Ranzato, R. Hadsell, M. F. Balcan, H. Lin, Eds. (Curran Associates, Inc., 2020), pp. 20852–20864.
47. T. Hoefler, D. Alistarh, T. Ben-Nun, N. Dryden, A. Peste, Sparsity in deep learning: pruning and growth for efficient inference and training in neural networks. *J. Mach. Learn. Res.* **22**, 10882–11005 (2021).
48. D. T. Campbell, Blind variation and selective retention in creative thought as in other knowledge processes. *Psychol. Rev.* **67**, 380–400 (1960).
49. S. N. Gomperts, F. Kloosterman, M. A. Wilson, VTA neurons coordinate with the hippocampal reactivation of spatial experience. *Elife* **4**, e05360 (2015).
50. G. Dragoi, S. Tonegawa, Preplay of future place cell sequences by hippocampal cellular assemblies. *Nature* **469**, 397–401 (2011).
51. J.-E. K. Miller, I. Ayzenshtat, L. Carrillo-Reid, R. Yuste, Visual stimuli recruit intrinsically generated cortical ensembles. *Proc. Natl. Acad. Sci. U. S. A.* **111**, E4053-61 (2014).
52. A. Luczak, P. Barthó, K. D. Harris, Spontaneous events outline the realm of possible sensory responses in neocortical populations. *Neuron* **62**, 413–425 (2009).
53. E. M. Izhikevich, *Dynamical systems in neuroscience: The geometry of excitability and bursting* (MIT Press, 2010).
54. Z. Brzosko, S. B. Mierau, O. Paulsen, Neuromodulation of spike-timing-dependent plasticity: Past, present, and future. *Neuron* **103**, 563–581 (2019).
55. Y. K. Wu, C. Miehl, J. Gjorgjieva, Regulation of circuit organization and function through inhibitory synaptic plasticity. *Trends Neurosci.* **45**, 884–898 (2022).
56. C. Q. Chiu, A. Barberis, M. J. Higley, Preserving the balance: diverse forms of long-term GABAergic synaptic plasticity. *Nat. Rev. Neurosci.* **20**, 272–281 (2019).
57. D. M. Blitz, K. A. Foster, W. G. Regehr, Short-term synaptic plasticity: a comparison of two synapses. *Nat. Rev. Neurosci.* **5**, 630–640 (2004).

58. R. E. Beaty, M. Benedek, P. J. Silvia, D. L. Schacter, Creative cognition and brain network dynamics. *Trends Cogn. Sci.* **20**, 87–95 (2016).
59. J. G. Klinzing, N. Niethard, J. Born, Mechanisms of systems memory consolidation during sleep. *Nat. Neurosci.* **22**, 1598–1610 (2019).
60. O. Barak, Recurrent neural networks as versatile tools of neuroscience research. *Curr. Opin. Neurobiol.* **46**, 1–6 (2017).
61. J. A. Acebrón, L. L. Bonilla, C. J. Pérez Vicente, F. Ritort, R. Spigler, The Kuramoto model: A simple paradigm for synchronization phenomena. *Rev. Mod. Phys.* **77**, 137–185 (2005).

Figures and Tables

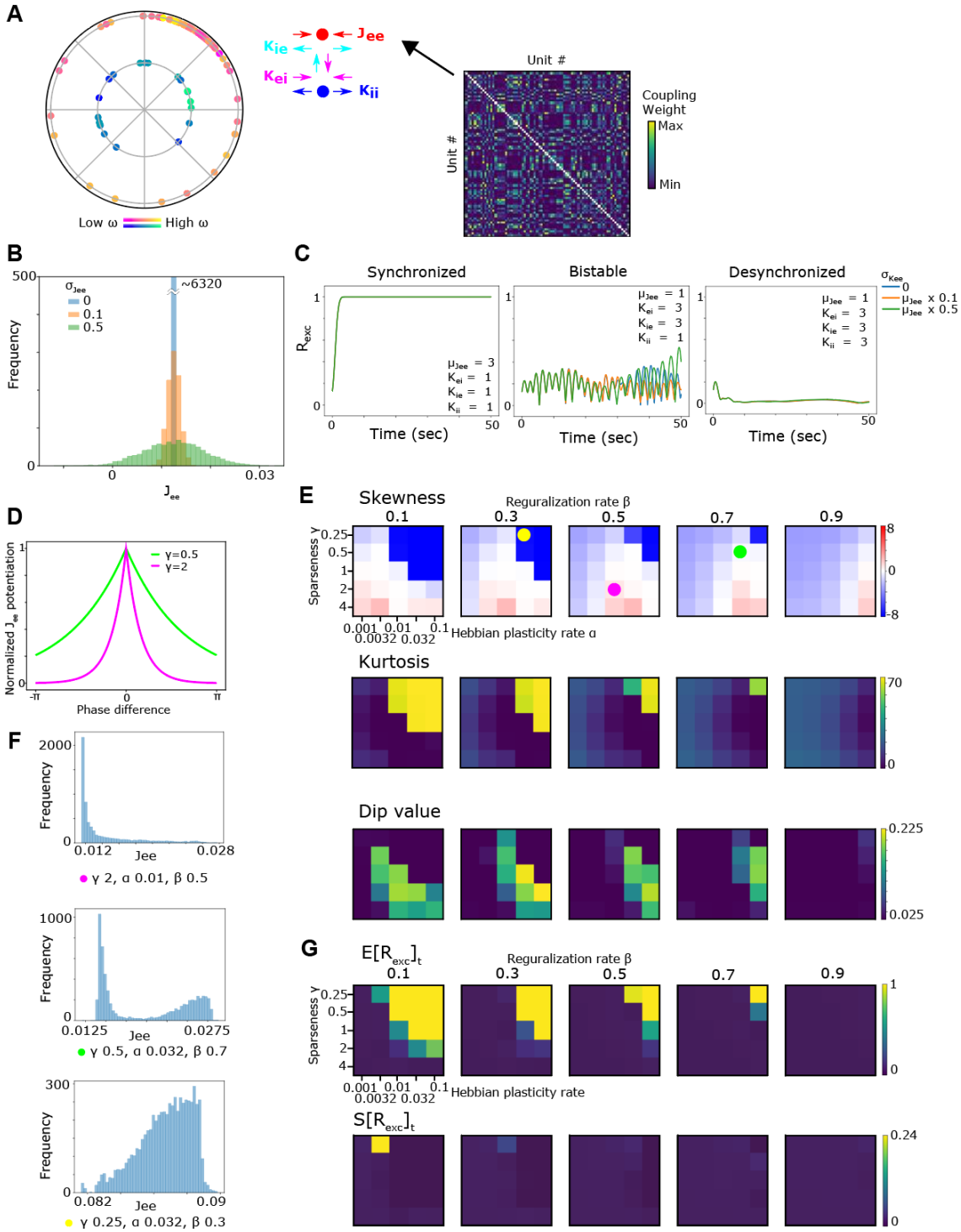

Figure 1. EI-Kuramoto model with distributed J_{ee} and plasticity

(A) Schematic representation of the pEI-Kuramoto model

Left: Oscillator units are excitatory (warm-colored) or inhibitory (cool-colored), each with its own natural frequency (shown by color gradients). Right: J_{ee} functions attractively between excUnits (red arrows), with each unit pair having its own coupling weight and undergoing plastic

modification (the right matrix). K_{ei} is the attractive interaction strength from excUnit to inhUnit (magenta arrow). K_{ii} is the repulsive strength between inhUnits (blue arrows). K_{ie} is the repulsive strength from inhUnit to excUnit (cyan arrow). K_{ei}, K_{ii}, and K_{ie} are constant and applied uniformly across all units. (B) Distribution of J_{ee} coupling weights with different σ_{Jee} $\mu_{Jee} = 1$, $N_{exc} = 80$. (C) R_{exc} time traces of synchronized, bistable, and desynchronized states with each σ_{Jee} (D) Exponential rules of Hebbian potentiation plasticity The J_{ee} weight of each pair of units is potentiated based on the phase difference between the units. (E) Validation of the J_{ee} distribution with various plasticity parameters Skewness (top panels), kurtosis (middle), and dip values (bottom). The parameters used for evaluation were $\mu_{Jee} = 1$, $\sigma_{Jee} = 0.1$, $K_{ei} = 3$, $K_{ie} = 3$, $K_{ii} = 3$, corresponding to a desynchronized state. (F) J_{ee} distribution of exponential Hebbian plasticity rules with various parameter settings The magenta, green, and yellow circles correspond to the parameter settings in (E). (G) Validation of the synchronization states with various plasticity parameters. $E[R_{exc}]_t$ and $S[R_{exc}]_t$ denote the time-averaged mean and standard deviation, respectively, of the order parameter for excUnits, R_{exc}.

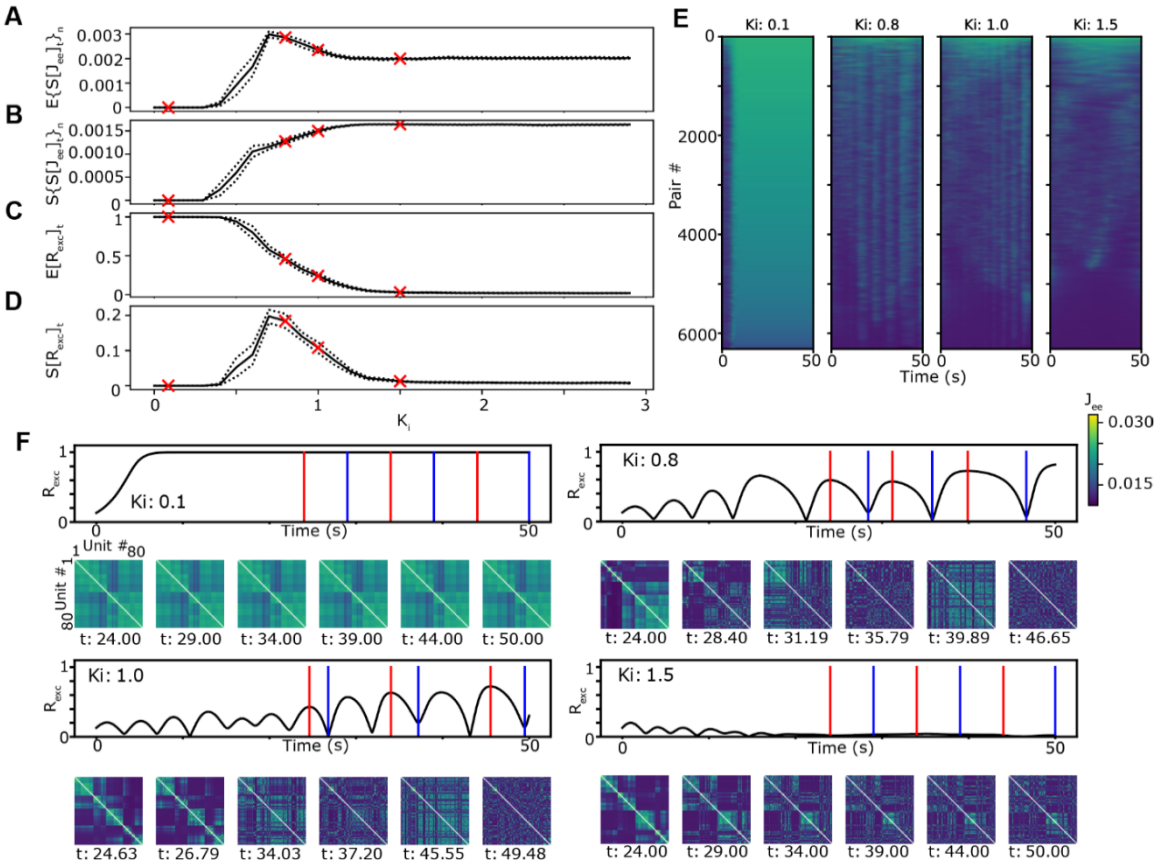

Figure 2. Changes in J_{ee} fluctuation with K_i modification

(A–D) (A) $E\{S[J_{ee}]_t\}_n$, (B) $S\{S[J_{ee}]_t\}_n$, (C) $E[R_{exc}]_t$, and (D) $S[R_{exc}]_t$ as a function of K_i Red crosses indicate each value in the K_i conditions shown in (E) and (F). (E) Time course of J_{ee} weights in different K_i conditions. The order of unit pairs is sorted by $E[J_{ee}]_t$ for each K_i value. (F) The upper panels show R_{exc} traces and time points of the left J_{ee} matrices. The red and blue vertical lines indicate the time points (red and blue are local maximum and local minimum, respectively, for K_i = 0.8 and 1.0; constant 5 s interval for K_i = 0.1 and 1.5). The lower panels show the J_{ee} weight matrix at selected time points (local minimum or maximum for K_i = 0.8 and 1.0, constant 5 s intervals for K_i = 0.1 and 1.5). The order of units is rearranged by the result of hierarchical clustering for the leftmost panel (around t: 24-25). E and F share the color bar.

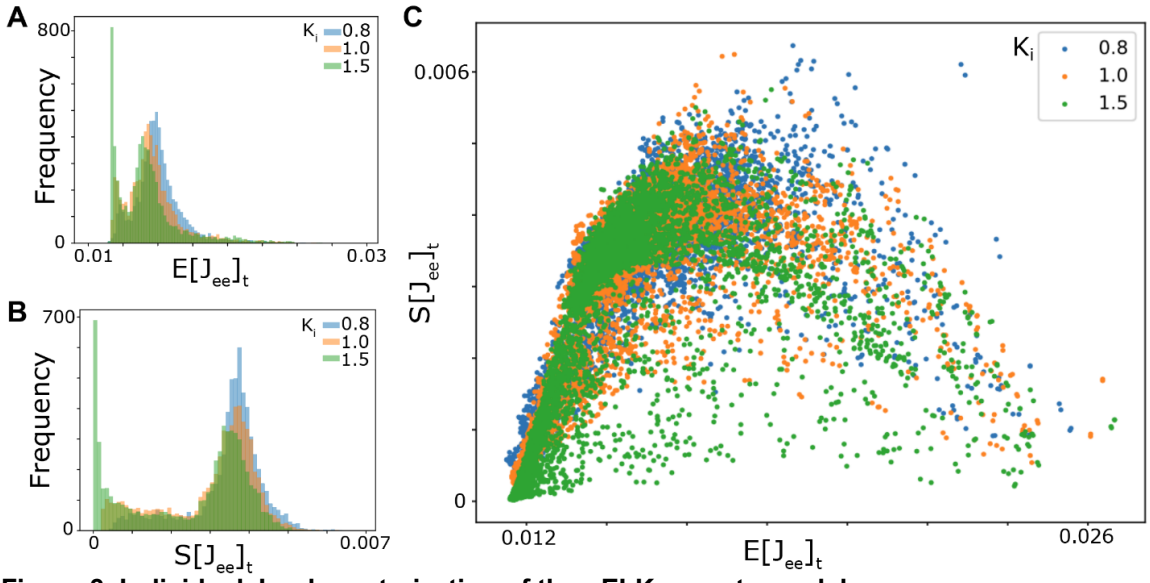

Figure 3. Individual J_{ee} characterization of the pEI-Kuramoto model
(A) $E[J_{ee}]_t$ histogram (B) $S[J_{ee}]_t$ histogram (C) $E[J_{ee}]_t$ vs. $S[J_{ee}]_t$ scatter plot for different K_i values

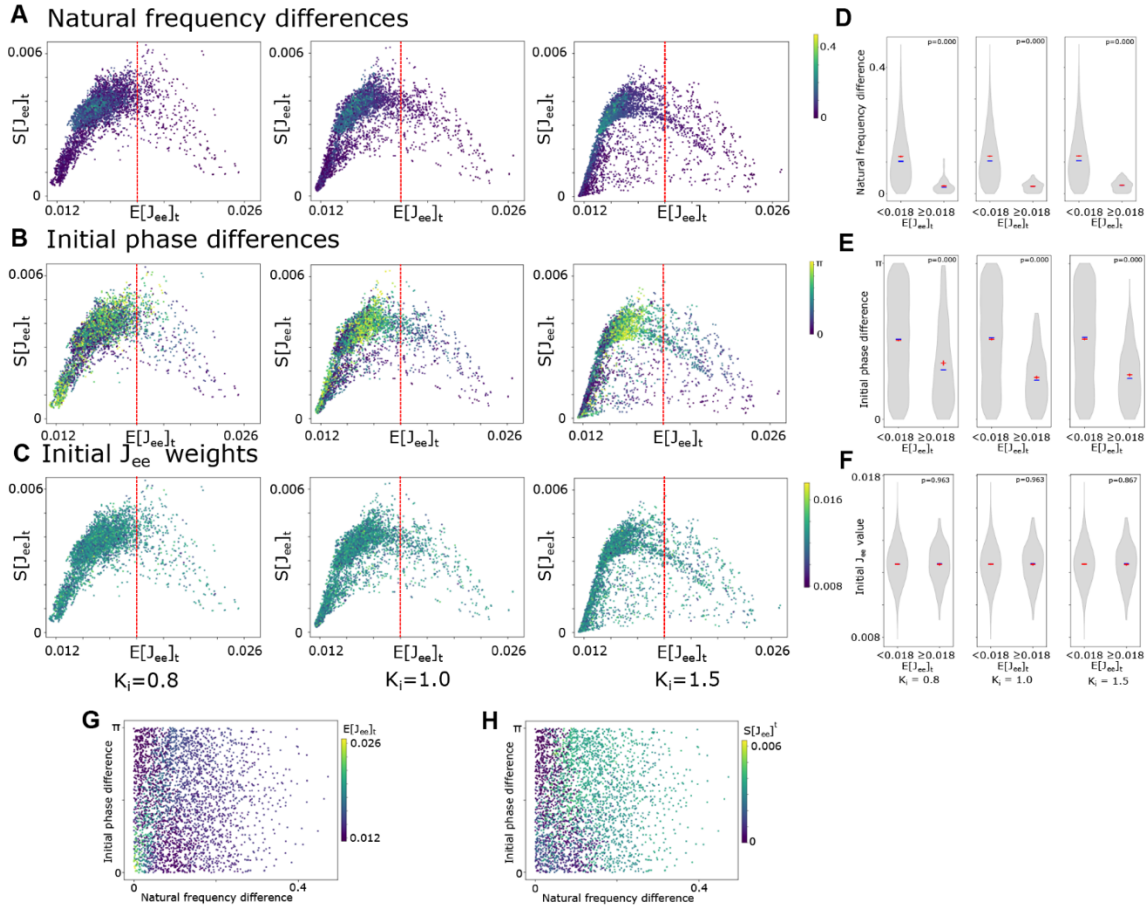

Figure 4. Factors for J_{ee} fluctuation

(A–C) $E[J_{ee}]_t$ vs. $S[J_{ee}]_t$ scatter plot with color coding of (A) the natural frequency ω_{exc} differences, (B) the initial phase differences, and (C) the initial J_{ee} weights over different K_i

The red dotted line in the upper left panel indicates $E[J_{ee}] = 0.018$. (D–F) Violin plots provide distribution densities based on whether the threshold $E[J_{ee}]_t \geq 0.18$ or not for (D) natural frequency ω_{exc} differences, (E) initial phase differences, and (F) initial J_{ee} weights across different K_i

The red and blue horizontal lines indicate the mean and median values, respectively. The red vertical lines indicate the standard errors. The numbers in the upper right corner of each panel are the p-values from the Mann–Whitney U test. (G and H) Scatter plots of natural frequency differences and initial phase differences with color coding of (G) $E[J_{ee}]_t$ and (H) $S[J_{ee}]_t$ (K_i = 1.5)

The Mann–Whitney U test was used for statistical analysis in panels D-F. The numbers of unit pairs were as follows: for K_i=0.8, <0.18: n=5968, ≥0.18: n=352; for K_i=1.0, <0.18: n=5920, ≥0.18: n=400; for K_i=1.5, <0.18: n=5852, ≥0.18: n=468. The statistics were as follows: (D, natural frequency difference), K_i=0.8, z=24.7, p<0.001; K_i=1.0, z=26.8, p<0.001; K_i=1.5, z=27.8, p<0.001. (E, initial phase difference) K_i=0.8, z=9.20, p<0.001; K_i=1.0, z=16.4, p<0.001; K_i=1.5, z=16.7, p<0.001. (F, initial J_{ee} weight) K_i=0.8, z=-0.046, p=0.96; K_i=1.0, z=0.046, p=0.96; K_i=1.5, z=0.17, p=0.87.

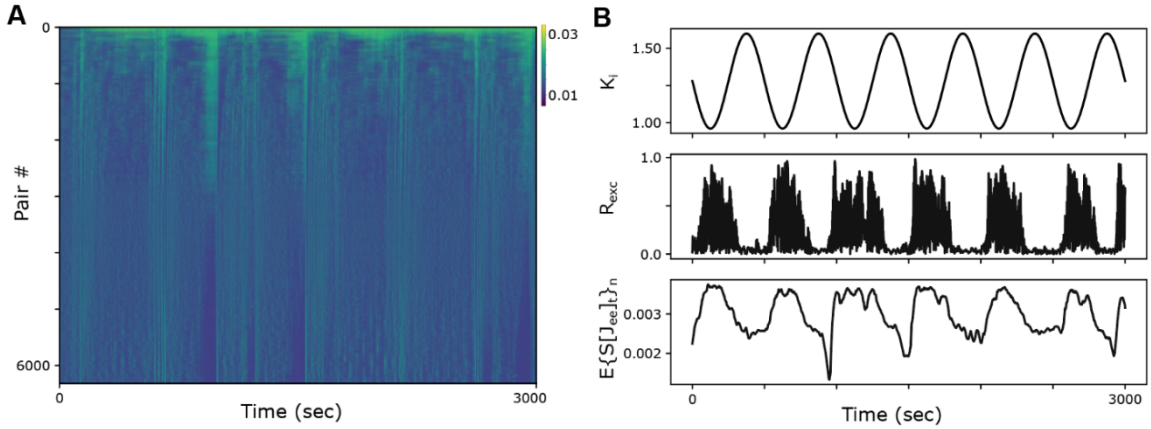

Figure 5. J_{ee} fluctuation changes with K_i cyclic modulation
(A) Time trace of each J_{ee} weight sorted by $E[J_{ee}]_t$. (B) Time traces of (top) K_i modulation, (middle) R_{exc}, and (low) $E\{S[J_{ee}]_t\}_n$

Supporting Information for
Synchronicity transitions determine coupling fluctuations in a model of coupled oscillators with plasticity

Satoshi Kuroki and Kenji Mizuseki

Satoshi Kuroki
Email: skuroki@omu.ac.jp

This PDF file includes:

Supporting text S1
Figures S1 to S3
Legends for Movies S1 to S5

Other supporting materials for this manuscript include the following:

Movies S1 to S5

Supporting Information Text

Text S1. Derivation of the quasi-steady coupling weight distribution

The combined changes from Hebbian and homeostatic plasticity (Eq M11 and M14) are summarized as follows:

$$J_{ee,kj}(t+\Delta t) = J_{ee,kj}(t) + \alpha \exp\left(-\gamma\left|\Delta\theta_{kj}\right|\right) - \beta\{J_{ee,kj}(t) + \alpha \exp\left(-\gamma\left|\Delta\theta_{kj}\right|\right) - \hat{J}_{Hebb}\} \quad \text{(S1)}.$$

Assuming quasi-steady J_{ee} distribution, $J_{ee,kj}(t+\Delta t) = J_{ee,kj}(t)$. If α is small enough, homeostatic set point attained after Hebbian potentiation $\hat{J}_{Hebb}$ can be approximated as that of before Hebbian potentiation, $\hat{J}_{Hebb} \approx \hat{J}_{ee,jk}$. Under these assumptions, the equation simplifies to:

$$\alpha(1-\beta)\exp\left(-\gamma\left|\Delta\theta_{kj}\right|\right) - \beta\left(J_{ee,kj} - \hat{J}_{ee,kj}\right) = 0 \quad \text{(S2)}.$$

Thus,

$$J_{ee,kj} = \hat{J}_{ee,kj} + c\exp\left(-\gamma\left|\Delta\theta_{kj}\right|\right) \quad \text{(S3)}.$$

$$c = \frac{\alpha(1-\beta)}{\beta}$$

This corresponds to Eq. 1 in the main text. The first term, $\hat{J}_{ee,kj}$, represents the homeostatic set point characterized by a J_{ee} distribution with mean $\hat{\mu}_{Jee}$ and variance $\hat{\sigma}_{Jee}$. This second term is the Hebbian potentiation component with a coefficient of $c = \alpha(1-\beta)/\beta$. Repeating this update, the J_{ee} distribution gradually reflects the influence of the Δθ-dependent Hebbian term.

We defined the probability density function (PDF) of the phases $f_\theta(\theta)$ assuming enough large number of units:

$$\int_0^{2\pi} f_\theta(\theta)d\theta = 1 \quad \text{(S4)}$$

The distribution of the phase difference, $f_{\Delta\theta}(\Delta\theta)$, between two independent phases is given by the circular autocorrelation of the phase distribution:

$$f_{\Delta\theta}(\Delta\theta) = \int_0^{2\pi} f_\theta(\theta)f_\theta(\theta+\Delta\theta)d\theta \ \ (-\pi \le \Delta\theta < \pi) \quad \text{(S5)}$$

In a fully desynchronized state, the phase distribution is uniform, $f(\theta) = 1/2\pi$. In this case, Eq. S5 becomes:

$$f_{\Delta\theta}(\Delta\theta) = \int_0^{2\pi} \frac{1}{2\pi}\cdot\frac{1}{2\pi}d\theta = \frac{1}{2\pi} \quad \text{(S6)}$$

This shows that the distribution of phase differences is also uniform. It follows that the distribution of the absolute phase difference, $x = |\Delta\theta| \sim \mathrm{Unif}(0,\pi)$, is a uniform distribution over [0,π], with a PDF:

$$f_{|\Delta\theta|}(x) = \frac{1}{\pi} \quad \text{(S7)}$$

Here, we evaluate $E[J_{ee}]$ and $S[J_{ee}]$ to calculate $\hat{J}_{ee,kj}$. We analyze the distribution of the Hebbian component from Eq. S3, $y = c\exp(-\gamma x)$, which is a transformation of the random variable x. Using this, the inverse transformation is:

$$x = -\frac{1}{\gamma}\log\frac{y}{c} \quad \text{(S9)}$$

The absolute value of the Jacobian of this transformation is:

$$\left|\frac{dx}{dy}\right| = \frac{1}{\gamma y} \quad \text{(S10)}$$

The relationship between the PDFs is given by $f_{|\Delta\theta|}(x)dx = f_{Jee}(y)dy$. Substituting the known quantities, we find the PDF for x:

$$f_{Jee}(y) = f_{|\Delta\theta|}(x)\left|\frac{dx}{dy}\right| = \frac{1}{\gamma\pi y} \ \ (y_{min} = ce^{-\gamma\pi} \le y \le y_{max} = c) \quad \text{(S12)}$$

Assuming the statistics of the full J_{ee} distribution are dominated by this Hebbian component in the desynchronized state, The mean $E[J_{ee}]$ and variance $Var[J_{ee}]$ is:

$$E[J_{ee}] = \int_{y_{min}}^{y_{max}} y f_{Jee}(y)dy = \int_{ce^{-\gamma\pi}}^{c} y\frac{1}{\gamma\pi y}dy = \frac{c(1-e^{-\pi\gamma})}{\gamma\pi} \quad \text{(S13)}$$

$$Var[J_{ee}] = E\left[{J_{ee}}^2\right] - (E[J_{ee}])^2 = \int_{ce^{-\gamma\pi}}^{c} y^2\frac{1}{\gamma\pi y}dy - (E[J_{ee}])^2 = \frac{c^2(1-e^{-2\pi\gamma})}{2\gamma\pi} - \left\{\frac{c(1-e^{-\pi\gamma})}{\gamma\pi}\right\}^2 \quad \text{(S14)}$$

Thus,

$$\hat{J}_{ee,kj} = \hat{\sigma}_{Jee}\left(\frac{j - E[J_{ee}]}{S[J_{ee}]}\right) + \hat{\mu}_{Jee}$$

$$\frac{x - E[J_{ee}]}{S[J_{ee}]} = \left[\frac{1}{\pi\gamma c\exp(-\gamma|\Delta\theta|)} - \frac{c(1-e^{-\pi\gamma})}{\gamma\pi}\right] \Big/ \left[\frac{c^2(1-e^{-2\pi\gamma})}{2\gamma\pi} - \left\{\frac{c(1-e^{-\pi\gamma})}{\gamma\pi}\right\}^2\right]^{\frac{1}{2}} \quad \text{(S15)}$$

Next, we considered the change in the phase difference for a pair of excUnits. Given Eq. M9 and S3, we calculate $d\Delta\theta_{kj}/dt = d\theta_k/dt - d\theta_j/dt$.

$$\frac{d\Delta\theta_{kj}}{dt} = \Delta\omega - 2\left\{\hat{J}_{ee,kj} + c\exp\left(-\gamma\left|\Delta\theta_{kj}\right|\right)\right\}\sin\left(\Delta\theta_{kj}\right) + F_{exc}^{(-kj)} - F_{inh} \quad \text{(S16)}$$

, where natural frequency difference $\Delta\omega = \omega_k - \omega_j$, repulsive force from the inhUnits $F_{inh} = -K_{ie}R_{inh}\{\sin(\theta_k - \psi_{inh}) - \sin\left(\theta_j - \psi_{inh}\right)\}$, and attractive force from the excUnits except unit k and j, $F_{exc}^{(-kj)}$. Under a mean-field approximation for sufficiently large number of units, this excitatory force term can be written as:

$$\begin{aligned} F_{exc}^{(-kj)} &= -\sum_{l\neq k,j}\left\{J_{ee,kl}\sin(\theta_k - \theta_l) - J_{ee,jl}\sin\left(\theta_j - \theta_l\right)\right\} \\ &\approx -J'^{(-kj)}_{ee}R_{exc}^{(-kj)}\left\{\sin\left(\theta_k - \psi_{exc}^{(-kj)}\right) - \sin\left(\theta_j - \psi_{exc}^{(-kj)}\right)\right\} \end{aligned} \quad \text{(S17)}$$

, where $J'^{(-kj)}_{ee}$ represents the effective attractive interaction strength on the pair from other excUnits. This system also reaches a steady state where $d\Delta\theta_{kj}/dt = 0$. Under this condition,

$$-\Delta\omega + F_{inh} - F_{exc}^{(-kj)} = -2\left\{\hat{J}_{ee,kj} + c\exp\left(-\gamma\left|\Delta\theta_{kj}\right|\right)\right\}\sin\left(\Delta\theta_{kj}\right) \quad \text{(S18)}$$

This corresponds to Eq. 2 in the main text. The right-hand side represents the interaction term between the excUnit k and j, while the left-hand side of this equation comprises all other influences, namely the natural frequency difference among the pair and the net mean-field force from the other units. A stable fixed point for $\Delta\theta_{kj}$ exists where the functions for the left and right-hand sides intersect (SI Appendix, Fig. S3). In the desynchronized state, the order parameters R_{exc}, R_{inh} are close to zero, limiting the influence of F_{inh} and $F_{exc}^{(-kj)}$. However, in the bistable state, these order parameters fluctuate periodically. This causes these forces to become influential, and as a result, the J_{ee} distribution is no longer in a quasi-steady state. Furthermore, the interaction term $\sin(\theta_k - \psi) - \sin\left(\theta_j - \psi\right)$ in F_{inh} and $F_{exc}^{(-kj)}$ is enhanced when the mean phase ψ lies on the shorter arc between θ_k and θ_j, but is weakened when it lies on the longer arc.

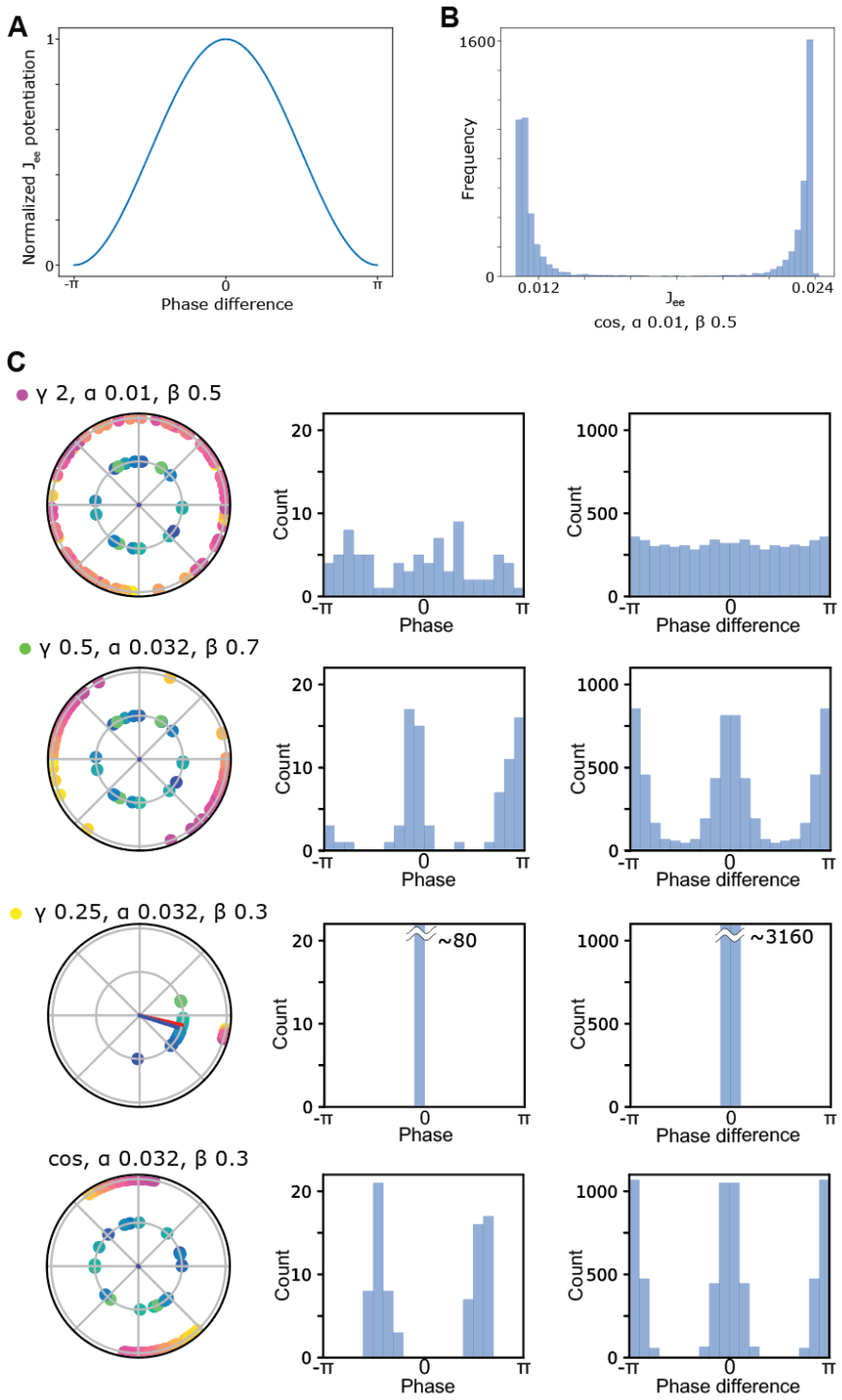

Fig. S1. Cosine Hebbian plasticity rule

(A) Cosine rule for the Hebbian potentiation plasticity. The J_{ee} weight of each pair of units is potentiated based on the phase difference between the units. (B) J_{ee} distribution using the cosine Hebbian plasticity rule. (C) Phase and phase difference distributions for each plasticity setting. Left panels: Polar plots showing the phases of excUnits (warm colors) and inhUnits (cool colors). Center panels: Histograms of the excUnit phases. Right panels: Histograms of the phase differences between pairs of excUnits.

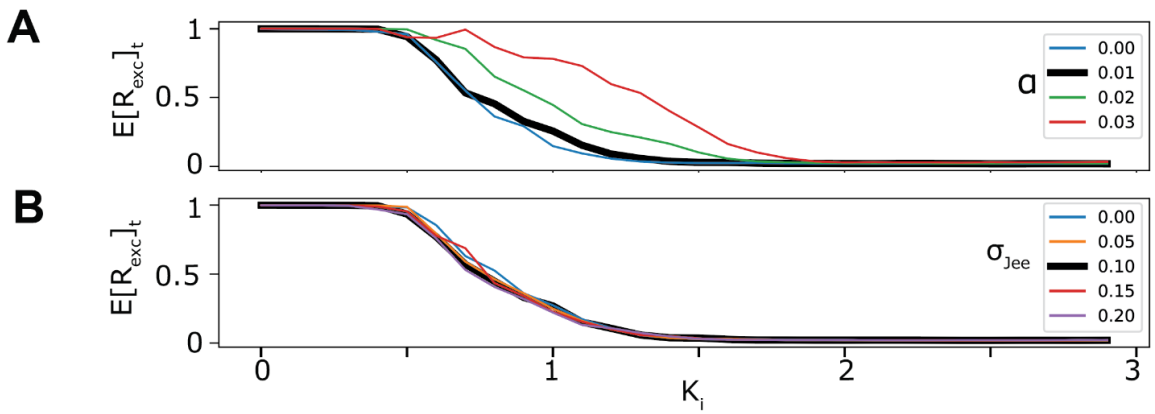

Fig. S2. Effect or Hebbian learning rate and J_{ee} variance for the synchronization

(A) $E[R_{exc}]_t$ as a function of K_i at different learning rates under Hebbian plasticity (α) settings
(B) $E[R_{exc}]_t$ as a function of K_i for different σ_{Jee} settings. The thick black lines are the same as those in Figure 2.

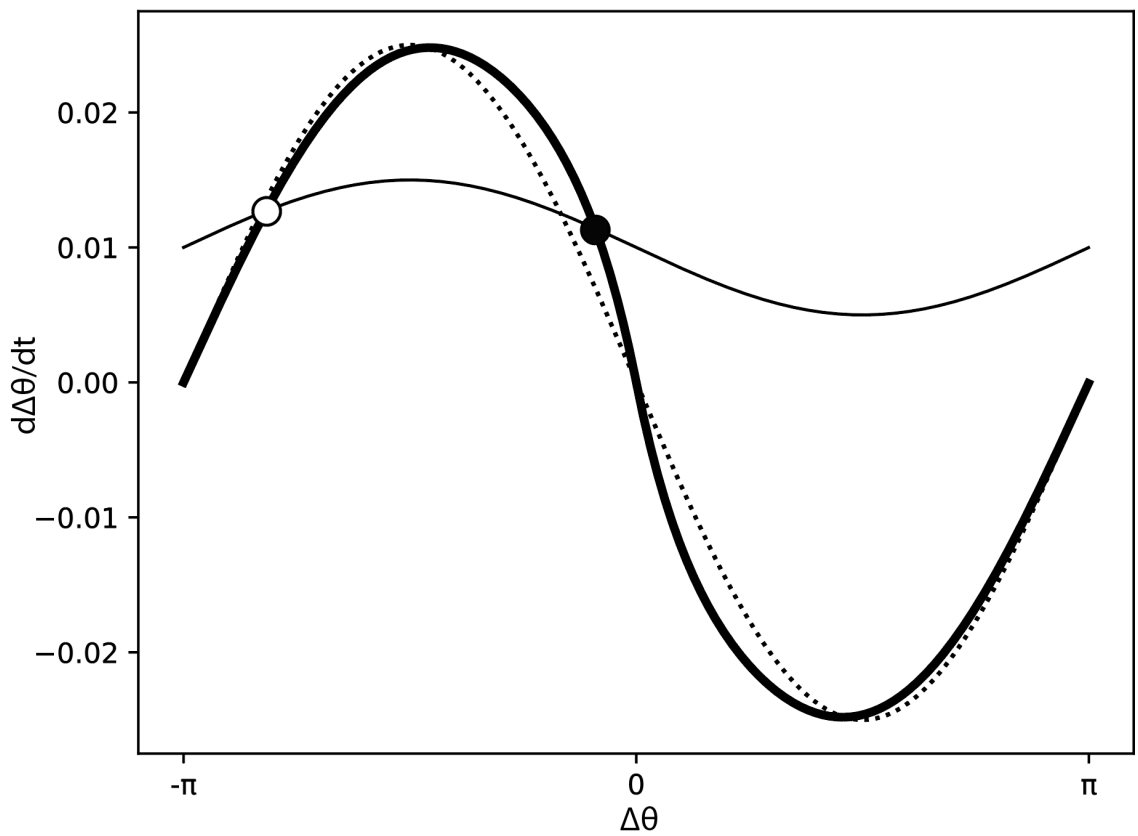

Fig. S3. Interaction function and equilibrium

The thick solid line indicates interaction function between excUnit pair $-2\left\{\hat{J}_{ee} + c\exp(-\gamma|\Delta\theta|)\right\}\sin(\Delta\theta)$. The thin solid line is total interaction strength from the other factors $-\Delta\omega + F_{inh} - F_{exc}^{(-kj)}$. The dot line indicates pure sine curve $\hat{\mu}_{Jee}\sin(\Delta\theta)$ for comparison. The black and white points indicate stable and unstable equilibrium, respectively. The parameter setting is α=0.01, β=0.5, γ=2, $\hat{\mu}_{Jee}$ =0.0125 ($\mu_{Jee}/\mathrm{N}_{exc}$= 1/80), $\hat{\sigma}_{Jee}$ = 0.00125 ($\sigma_{Jee}/\mathrm{N}_{exc}$= 0.1/80) (Fig 1F magenta). $\Delta\omega$ = -0.01, $F_{inh} - F_{exc}^{(-kj)} = -0.2\sin\Delta\theta$.

Movie S1 (separate file) Synchronized state: μ_{Jee} = 1, σ_{Jee} = 0.1, K_{ei}=3, K_{ie}=0.1, K_{ii}=0.1, γ=2, α=0.01, β=0.5; playback speed: ×1

Movie S2 (separate file) Desynchronized state: μ_{Jee} = 1, σ_{Jee} = 0.1, K_{ei}=3, K_{ie}=1.5, K_{ii}=1.5, γ=2, α=0.01, β=0.5; playback speed: ×1

Movie S3 (separate file) Bistable state1: μ_{Jee} = 1, σ_{Jee} = 0.1, K_{ei}=3, K_{ie}=0.8, K_{ii}=0.8, γ=2, α=0.01, β=0.5; playback speed: ×1

Movie S4 (separate file) Bistable state2: μ_{Jee} = 1, σ_{Jee} = 0.1, K_{ei}=1, K_{ie}=1, K_{ii}=1, γ=2, α=0.01, β=0.5; playback speed: ×1

Movie S5 (separate file) Cyclic inhibitory modulation, K_i, playback speed ×20